IMA Journal of Applied Mathematics (2010) **75**, 525–548
doi:10.1093/imamat/hxq020
Advance Access publication on April 22, 2010

Plane strain bifurcations of elastic layered structures subject to finite bending: theory versus experiments

S. ROCCABIANCA, M. GEI AND D. BIGONI*
Department of Mechanical and Structural Engineering, University of Trento, Via Mesiano 77, I-38123 Trento, Italy
*Corresponding author: bigoni@ing.unitn.it

[Received on 27 August 2009; Revised on 6 November 2009; accepted on 18 March 2010]

Finite plane strain bending is solved for a multilayered elastic–incompressible thick plate. This multilayered solution, previously considered only in the case of homogeneity, is in itself interesting and reveals complex stress states such as the existence of more than one neutral axis for certain geometries. The bending solution is employed to investigate possible incremental bifurcations. The analysis reveals that a multilayered structure can behave in a completely different way from the corresponding homogeneous plate. For a thick plate of neo-Hookean material, for instance, the presence of a stiff coating strongly affects the bifurcation critical angle. Experiments designed and performed to substantiate our theoretical findings demonstrate that the theory can be effectively used as a design tool for predicting the capability of an elastic multilayered structure to be subject to a finite bending without suffering localized crazing.

Keywords: non-linear elasticity, neutral axes.

1. Introduction

Finite bending of plates is a phenomenon common in nature[1] and in engineered processes.[2] Although *plates suffering finite bending are often made up of layers*,[3] the theory of finite elastic bending has been developed only under the assumption of homogeneity (Rivlin, 1949; Truesdell & Toupin, 1960; Green & Zerna, 1968; Lurie, 2005) . Moreover, while certain elastic multilayers can be bent until the tubular shape is reached without any appearance of inhomogeneities, crazes develop for other systems (Fig. 1 and also Fig. 14), severely decreasing the elastic deformational capability.

Since these crazes can be interpreted as bifurcation modes localized near the surface, the bifurcation analysis becomes an important tool for design purposes. However, theoretical (Triantafyllidis, 1980; Dryburgh & Ogden, 1999; Haughton, 1999; Bruhns *et al.*, 2002, 2003; Coman & Destrade, 2008) and experimental (Gent & Cho, 1999) approaches to bifurcation of plates subject to finite bending have

[1]For instance, leaves are often subject to large bending for various reasons: the *Pinguicula leptoceras* curls its leaf to trap insects, the *Geranium pratense*'s pod suffers a strong bending when seeds are dispersed, and *gramineae* leaves deform into a tube to resist dehydratation. Moreover, arteries unfold when cut longitudinally, thus showing that the internal stress state developed during morphogenesis is compatible with a finite bending.

[2]Bending is important in metalworking techniques and tissue-engineered blood vessels in which the internal fibroblast sheets are 'wrapped' around a tubular support (L'Heureux *et al.*, 2006). In microelectronic devices, we may mention that flexible solar cells (made up of layers, one of which containing 3D nanopillar-array photovoltaics) have a 4 mm thickness and are subject to bending up to a curvature radius of 3 cm (Fan *et al.*, 2009).

[3]Leaves, arteries and the flexible solar cells (Fan *et al.*, 2009) are complex structures composed of at least three layers.

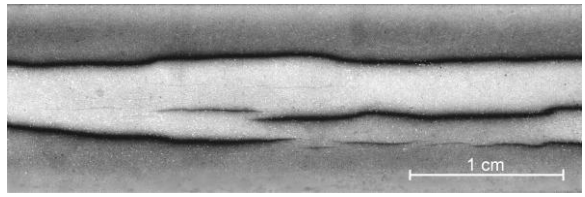

FIG. 1. Crazes on the surface of a rubber strip subject to finite bending.

only been considered under the assumption of material homogeneity. Therefore, the aims of the present article are

(i) to provide an analytical solution to finite bending of an elastic multilayered thick plate deformed under the plane strain constraint;
(ii) to analyse and solve the problem of 2D bifurcations possibly occurring during bending;
(iii) to validate our theoretical approach with experiments.

The solution for finite bending of an elastic multilayer discloses the complex stress distributions that can be generated inside such structures as a result of large strains. For instance, *more than one neutral axis* may be present[4] (Fig. 5) and weakly stressed layers may 'bond' a highly stressed one (Fig. 6). The determination of these stress states is of great importance in the design of multilayered structures, but then the question arises if such configurations can be achieved without encountering a previous bifurcation. In fact, one conclusion of the bifurcation analysis is that there is a strong difference between bifurcation loads and geometries when homogeneous structures are compared with the corresponding layered structures. For instance, a stiff and thin coating reinforcing an elastic layer strongly decreases the bifurcation bending angle of the uncoated structure, a finding fully consistent with the solutions obtained employing a surface coating model by Dryburgh & Ogden (1999) and Gei & Ogden (2002).

Experimentally, bifurcations of homogeneous elastic strips subject to bending have been investigated only by Gent & Cho (1999), although the experimental setting is not particularly complex. To extend their analyses to the case of layered plates, we have designed a simple device to impose a bending angle to elastic strips on which bifurcations in the form of crazes can be detected by direct visual inspection. To highlight our findings, we anticipate our experimental results (that will be detailed in Section 7) in Fig. 2, where the critical bending semi-angle ($\bar{\theta}_{\rm cr}$) at bifurcation is reported versus the aspect ratio of the samples (three uncoated rubber strips and ten coated strips with two coatings always situated at the tensile side of the structure). Experiments reveal that the trend predicted by the theory[5] is qualitatively very well followed, while quantitatively experimental values of the bifurcation angles result often sligthly lower than the theoretical predictions (a result consistent with the observations by

[4]In our examples, we have found situations with two (Fig. 4) and three (Fig. 5) neutral axes. More than one neutral axis can occur as induced in a multilayer by thermal loadings or residual stresses (see Chu, 1998; Chuang & Lee, 2000), in our context they occur under pure bending loading as a consequence of large strains.

[5]Surprisingly, the fact that the critical angle at bifurcation $\bar{\theta}_{\rm cr}$ versus the initial aspect ratio l_0/h_0 for an (uncoated) elastic thick plate is well approximated by a straight line and yields the simple formula (54) has passed unnoted until now. Unfortunately, the situation for multilayers is more complicated and linear approximations are possible only in special cases, for instance, those reported in Fig. 2, but not that reported in Fig. 8.

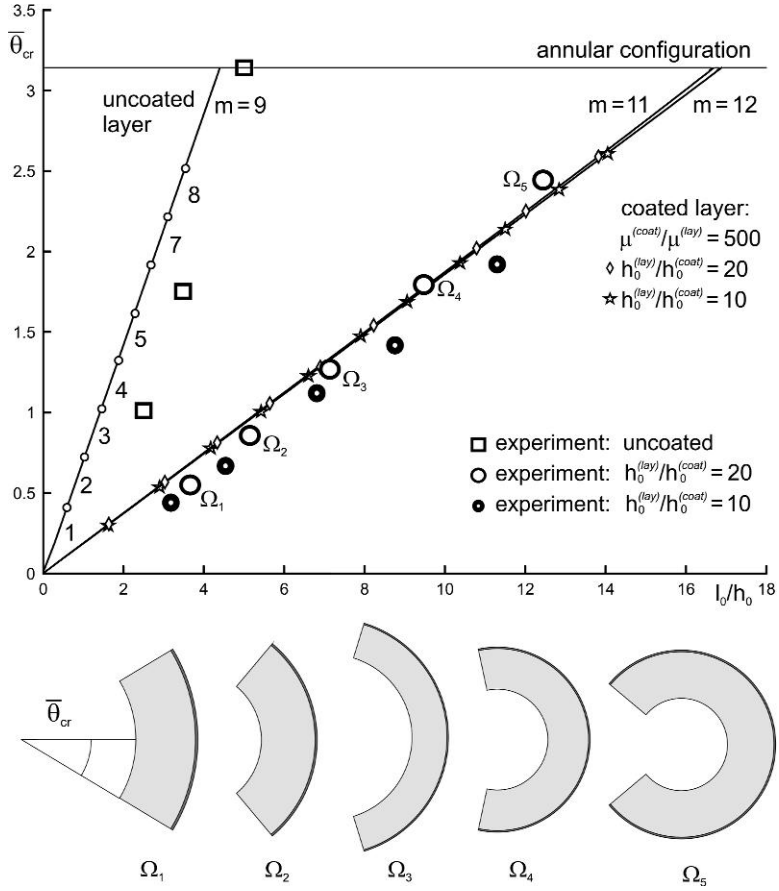

FIG. 2. Experimental results versus theoretical predictions for the bifurcation opening semi-angle $\bar{\theta}_{\rm cr}$ of uncoated and coated rubber strips subject to finite bending versus the aspect ratio l_0/h_0 of the undeformed configuration. Theoretical predictions for neo-Hookean materials are indicated with solid lines marked with 'diamonds', 'stars' or 'small circles', denoting transitions between values of the parameter m setting the circumferential wave number of the bifurcation mode, equation (53). The shear moduli ratio $\mu^{(\rm coat)}/\mu^{(\rm lay)}$ of the coated layers has been taken equal to 500, while two thickness ratios $h_0^{(\rm lay)}/h_0^{(\rm coat)}$ equal to 20 and 10 have been considered. The critical theoretical configurations (for $h_0^{(\rm lay)}/h_0^{(\rm coat)} = 20$) corresponding to bifurcation points Ω_i $(i = 1, \ldots, 4)$ are sketched in the lower part of the figure.

Gent & Cho, 1999). The fact that experimental results substantiate theoretical predictions allows us to conclude that bifurcation theory can be successfully employed to predict the deformational capabilities of a composite plate subject to finite bending.

2. Notation and governing equations

The notation employed throughout the present article and the main equations governing equilibrium in finite and incremental elasticity are now briefly recalled. Let $\boldsymbol{x}^0$ denote the position of a material point in some stress-free reference configuration B_0 of an elastic body. A deformation $\boldsymbol{\xi}$ is applied, mapping points of B_0 to those of the current configuration B indicated by $\boldsymbol{x} = \boldsymbol{\xi}(\boldsymbol{x}^0)$. We identify its deformation

gradient by $\boldsymbol{F}$, i.e. $\boldsymbol{F} = \mathrm{Grad}\boldsymbol{\xi}$, and we define the right, $\boldsymbol{C}$, and the left, $\boldsymbol{B}$, Cauchy–Green tensors as $\boldsymbol{C} = \boldsymbol{F}^{\top}\boldsymbol{F}$ and $\boldsymbol{B} = \boldsymbol{F}\boldsymbol{F}^{\top}$.

For isotropic incompressible elasticity, the constitutive equations can be written as a relationship between the Cauchy stress $\boldsymbol{T}$ and $\boldsymbol{B}$ as

$$\boldsymbol{T} = -\pi\boldsymbol{I} + \alpha_1\boldsymbol{B} + \alpha_{-1}\boldsymbol{B}^{-1}, \quad \det\boldsymbol{B} = 1, \tag{1}$$

where π is an arbitrary Lagrangian multiplier representing a hydrostatic pressure and $\alpha_1$and α_{-1} are coefficients which may depend on the deformation.

Alternatively, the principal stresses T_i $(i = 1, 2, 3)$, that are aligned with the Eulerian principal axes, can be obtained in terms of a strain-energy function W, which can be viewed as a function of the principal stretches λ_i $(i = 1, 2, 3)$. In the case of an incompressible material, these relationships take the form (index i not summed)

$$T_i = -\pi + \lambda_i\frac{\partial W(\lambda_1, \lambda_2, \lambda_3)}{\partial\lambda_i}, \quad \lambda_1\lambda_2\lambda_3 = 1. \tag{2}$$

Equations (1) and (2) are linked through (Bigoni & Gei, 2001):

$$\begin{aligned}\alpha_1 &= \frac{1}{\lambda_1^2 - \lambda_2^2}\left[\frac{(T_1 - T_3)\lambda_1^2}{\lambda_1^2 - \lambda_3^2} - \frac{(T_2 - T_3)\lambda_2^2}{\lambda_2^2 - \lambda_3^2}\right],\\ \alpha_{-1} &= \frac{1}{\lambda_1^2 - \lambda_2^2}\left[\frac{T_1 - T_3}{\lambda_1^2 - \lambda_3^2} - \frac{T_2 - T_3}{\lambda_2^2 - \lambda_3^2}\right],\end{aligned} \tag{3}$$

that allow to express coefficients α_1 and α_{-1} in terms of the strain energy of the body.

In the absence of body forces, equilibrium is expressed in terms of the first Piola–Kirchhoff stress tensor $\boldsymbol{S} = J\boldsymbol{T}\boldsymbol{F}^{-\top}$ as $\mathrm{Div}\boldsymbol{S} = \boldsymbol{0}$.

Loss of uniqueness of the plane-strain incremental boundary-value problem is investigated, so that incremental displacements are given by

$$\boldsymbol{u}(\boldsymbol{x}) = \dot{\boldsymbol{\xi}}(\boldsymbol{x}^0), \tag{4}$$

where, as in the following, a superposed dot is used to denote a first-order increment. The incremental counterpart of equilibrium is expressed by $\mathrm{div}\boldsymbol{\Sigma} = \boldsymbol{0}$, where the updated incremental first Piola–Kirchhoff stress is given by

$$\boldsymbol{\Sigma} = \dot{\boldsymbol{S}}\boldsymbol{F}^{\top}, \quad \dot{\boldsymbol{S}} = \dot{\boldsymbol{T}}\boldsymbol{F}^{-\top} - \boldsymbol{T}\boldsymbol{L}^{\top}\boldsymbol{F}^{-\top}. \tag{5}$$

The linearized constitutive equation is

$$\boldsymbol{\Sigma} = \mathbb{C}\boldsymbol{L} - \dot{\pi}\boldsymbol{I}, \tag{6}$$

where $\boldsymbol{L} = \mathrm{grad}\boldsymbol{u}$ and $\mathbb{C}$ is the fourth-order tensor of instantaneous elastic moduli (possessing the major symmetries). Incompressibility requires that $\mathrm{tr}\boldsymbol{L} = 0$. Since $\boldsymbol{\Sigma} = \dot{\boldsymbol{T}} - \boldsymbol{T}\boldsymbol{L}^{\top}$, the balance of rotational momentum yields $\Sigma_{12} - \Sigma_{21} = T_2L_{12} - T_1L_{21}$ and a comparison with (6) shows that (no sum on indices i and j)

$$\mathbb{C}_{ijji} + T_i = \mathbb{C}_{jiji} \quad (i \neq j). \tag{7}$$

For a hyperelastic material, the components of $\mathbb{C}$ can be defined in terms of the strain-energy function W. For the plane problem addressed here, their explicit form will be given in Section 5.

3. Finite pure bending of an elastic layered block

The solution for pure bending of an elastic layered thick plate made up of N layers follows from 'assembling' solutions relative to the bending of all layers taken separately, a solution first given by Rivlin (1949). Therefore, we begin recalling this solution now with reference to a generic layer, denoted as the sth. To this purpose, we consider plane-strain flexure of an incompressible rectangular elastic layered plate of initial dimensions $l_0 \times h_0$ (see Fig. 3(b)).

3.1 *Kinematics*

In the reference stress-free configuration, a Cartesian coordinate system $O_0^{(s)} x_1^{0(s)} x_2^{0(s)} x_3^{0(s)}$ is introduced for each layer, centred at its centroid (see Fig. 3(a)). Denoting by $\boldsymbol{e}_i^0$ $(i = 1, 2, 3)$ the common cartesian basis, the position of the generic point $\boldsymbol{x}^{0(s)}$ is given by

$$\boldsymbol{x}^{0(s)} = x_1^{0(s)} \boldsymbol{e}_1^0 + x_2^{0(s)} \boldsymbol{e}_2^0 + x_3^{0(s)} \boldsymbol{e}_3^0, \tag{8}$$

with

$$x_1^{0(s)} \in [-h_0^{(s)}/2, h_0^{(s)}/2], \quad x_2^{0(s)} \in [-l_0/2, l_0/2], \quad x_3^{0(s)} \in (-\infty, +\infty). \tag{9}$$

The deformed configuration is a portion of a cylindrical tube of semi-angle $\bar{\theta}$. It is useful to introduce here a cylindrical coordinate system $O^{(s)} r^{(s)} \theta^{(s)} z^{(s)}$, with basis $\boldsymbol{e}_r$, $\boldsymbol{e}_\theta$ and $\boldsymbol{e}_z$, where points of the sth layer are transformed to points identified by

$$r^{(s)} \in [r_i^{(s)}, r_i^{(s)} + h^{(s)}], \quad \theta^{(s)} \in [-\bar{\theta}, +\bar{\theta}], \quad z^{(s)} \in (-\infty, +\infty).$$

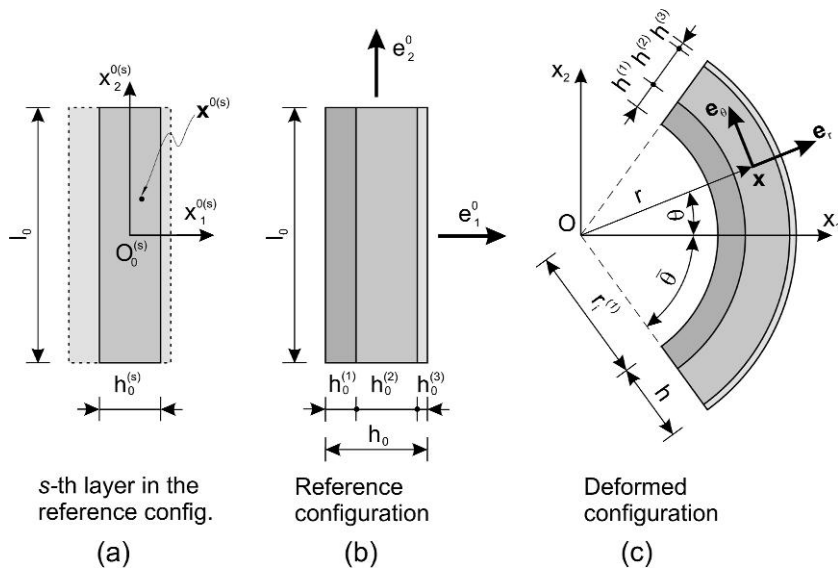

FIG. 3. Sketch of a generic layered thick plate subject to finite bending.

The deformation is prescribed in a way that a plane at constant $x_1^{0(s)}$ transforms to a circular arc at constant $r^{(s)}$, while a plane at constant $x_2^{0(s)}$ transforms to a plane at constant $\theta^{(s)}$. The out-of-plane deformation is null, so that $x_3^{0(s)} = z^{(s)}$. The incompressibility constraint (conservation of areas) imposes that

$$r_i^{(s)} = \frac{l_0 h_0^{(s)}}{2\bar{\theta} h^{(s)}} - \frac{h^{(s)}}{2}, \tag{10}$$

where $h^{(s)}$ is the current thickness of the circular sector, to be determined. The deformation, in this condition, is described by functions

$$r^{(s)} = r^{(s)}(x_1^{0(s)}), \quad \theta^{(s)} = \theta^{(s)}(x_2^{0(s)}), \quad z^{(s)} = x_3^{0(s)}, \tag{11}$$

so that the deformation gradient takes the form

$$\boldsymbol{F}^{(s)} = \frac{\mathrm{d}r^{(s)}}{\mathrm{d}x_1^{0(s)}} \boldsymbol{e}_r \otimes \boldsymbol{e}_1^0 + r^{(s)} \frac{\mathrm{d}\theta^{(s)}}{\mathrm{d}x_2^{0(s)}} \boldsymbol{e}_\theta \otimes \boldsymbol{e}_2^0 + \boldsymbol{e}_z \otimes \boldsymbol{e}_3^0. \tag{12}$$

The right and left Cauchy–Green tensors are

$$\begin{aligned} \boldsymbol{C}^{(s)} &= \left(\frac{\mathrm{d}r^{(s)}}{\mathrm{d}x_1^{0(s)}} \right)^2 \boldsymbol{e}_1^0 \otimes \boldsymbol{e}_1^0 + \left(r^{(s)} \frac{\mathrm{d}\theta^{(s)}}{\mathrm{d}x_2^{0(s)}} \right)^2 \boldsymbol{e}_2^0 \otimes \boldsymbol{e}_2^0 + \boldsymbol{e}_3^0 \otimes \boldsymbol{e}_3^0, \\ \boldsymbol{B}^{(s)} &= \left(\frac{\mathrm{d}r^{(s)}}{\mathrm{d}x_1^{0(s)}} \right)^2 \boldsymbol{e}_r \otimes \boldsymbol{e}_r + \left(r^{(s)} \frac{\mathrm{d}\theta^{(s)}}{\mathrm{d}x_2^{0(s)}} \right)^2 \boldsymbol{e}_\theta \otimes \boldsymbol{e}_\theta + \boldsymbol{e}_z \otimes \boldsymbol{e}_z, \end{aligned} \tag{13}$$

so that we identify the principal stretches to be

$$\lambda_r^{(s)} = \frac{\mathrm{d}r^{(s)}}{\mathrm{d}x_1^{0(s)}}, \quad \lambda_\theta^{(s)} = r^{(s)} \frac{\mathrm{d}\theta^{(s)}}{\mathrm{d}x_2^{0(s)}} \quad \text{and} \quad \lambda_z^{(s)} = 1. \tag{14}$$

Imposition of the incompressibility constraint reduces the deformation to the simple form

$$r^{(s)} = \sqrt{\frac{2}{\alpha^{(s)}} x_1^{0(s)} + \beta^{(s)}}, \quad \theta^{(s)} = \alpha^{(s)} x_2^{0(s)}, \tag{15}$$

so that, using (11), the principal stretches can be evaluated as

$$\lambda_r^{(s)} = \frac{1}{\alpha^{(s)} r^{(s)}}, \quad \lambda_\theta^{(s)} = \alpha^{(s)} r^{(s)} \quad \text{and} \quad \lambda_z^{(s)} = 1, \tag{16}$$

where $\alpha^{(s)}$ and $\beta^{(s)}$ are constants which are fixed by boundary conditions. For the sth layer of a multilaminated, these are

- at $x_2^{0(s)} = \pm l_0/2$, $\theta^{(s)} = \pm\bar{\theta}$; from $(15)_2$, $\theta^{(s)} = \pm\alpha^{(s)} l_0/2$, yielding

$$\alpha^{(s)} = \frac{2\bar{\theta}}{l_0}; \tag{17}$$

note that $\alpha^{(s)}$ is independent of the index s;

- at $x_1^{0(s)} = -h_0^{(s)}/2$, $r^{(s)} = r_i^{(s)}$; from (10) and $(15)_1$, $r_i^{(s)} = r^{(s)}(-h_0^{(s)}/2)$, yielding

$$\beta^{(s)} = r_i^{(s)^2} + \frac{l_0 h_0^{(s)}}{2\bar{\theta}}. \tag{18}$$

Since the N layers are assumed to be perfectly bonded to each other and the sth layer has current thickness $h^{(s)}$, we have

$$r_i^{(s)} = r_i^{(s-1)} + h^{(s-1)} \quad (s = 2, \ldots, N), \tag{19}$$

with $r_i^{(1)}$ given by $r_i^{(1)} = l_0 h_0^{(1)}/(2\bar{\theta}h^{(1)}) - h^{(1)}/2$ (see (10)). A repeated use of (10) and (19) provides all thicknesses $h^{(s)}$ $(s = 2, \ldots, N)$ expressed in terms of the thickness of the first layer $h^{(1)}$, which remains the sole kinematical unknown of the problem, determined from the solution of the boundary-value problem described in Section 3.2.

Since (19) is imposed at each of the $N - 1$ interfaces between layers, all radial coordinates $r^{(s)}$ share the same origin O of a new cylindrical coordinate system $Or\theta z$, common to all deformed layers (Fig. 3(c)); therefore, index s on the local current coordinates will be omitted in the following so that the deformed configuration will be described in terms of the global system $Or\theta z$.

As a conclusion, the kinematics provides all the stretches in the multilayered which can be represented as

$$\lambda_r = \frac{l_0}{2\bar{\theta}r}, \quad \lambda_\theta = \frac{2\bar{\theta}r}{l_0} \quad \text{and} \quad \lambda_z = 1, \tag{20}$$

and the current thickness of the sth layer, $h^{(s)}$, as a function of $h^{(s-1)}$, namely

$$h^{(s)} = -\frac{l_0 h_0^{(s-1)}}{2\bar{\theta}h^{(s-1)}} - \frac{h^{(s-1)}}{2} + \sqrt{\left(\frac{l_0 h_0^{(s-1)}}{2\bar{\theta}h^{(s-1)}} + \frac{h^{(s-1)}}{2}\right)^2 - \frac{l_0 h_0^{(s)}}{\bar{\theta}}} \quad (s = 2, \ldots, N). \tag{21}$$

Therefore, all current thicknesses are known once the thickness of the first layer, $h^{(1)}$, is known.

3.2 *Stress*

We are now in a position to determine the stress state within the multilayer. In particular, the Cauchy stress tensor in generic layer s can be written as

$$\boldsymbol{T}^{(s)} = T_r^{(s)} \boldsymbol{e}_r \otimes \boldsymbol{e}_r + T_\theta^{(s)} \boldsymbol{e}_\theta \otimes \boldsymbol{e}_\theta + T_z^{(s)} \boldsymbol{e}_z \otimes \boldsymbol{e}_z, \tag{22}$$

where, from the constitutive equations (2),

$$T_r^{(s)} = -\pi^{(s)} + \lambda_r \frac{\partial W^{(s)}}{\partial \lambda_r}, \quad T_\theta^{(s)} = -\pi^{(s)} + \lambda_\theta \frac{\partial W^{(s)}}{\partial \lambda_\theta}, \tag{23}$$

$$T_z^{(s)} = -\pi^{(s)} + \left.\frac{\partial W^{(s)}}{\partial \lambda_z}\right|_{\lambda_z = 1}.$$

Since stretches depend only on r, the chain rule of differentiation

$$\frac{\mathrm{d}\cdot}{\mathrm{d}r} = \frac{\partial\cdot}{\partial\lambda_r}\frac{\mathrm{d}\lambda_r}{\mathrm{d}r} + \frac{\partial\cdot}{\partial\lambda_\theta}\frac{\mathrm{d}\lambda_\theta}{\mathrm{d}r}, \tag{24}$$

together with (23) and the derivatives of stretches with respect to r calculated from (16), can be used in the equilibrium equations

$$\frac{\partial T_r^{(s)}}{\partial r} + \frac{T_r^{(s)} - T_\theta^{(s)}}{r} = 0, \quad \frac{\partial T_\theta^{(s)}}{\partial \theta} = 0 \tag{25}$$

to obtain the identities

$$\frac{\mathrm{d}W^{(s)}}{\mathrm{d}r} = -\frac{T_r^{(s)} - T_\theta^{(s)}}{r} = \frac{\mathrm{d}T_r^{(s)}}{\mathrm{d}r}. \tag{26}$$

Therefore, identifying λ_θ with λ, we arrive at the expression

$$T_r^{(s)}(r) = \hat{W}^{(s)}(\lambda(r)) + \gamma^{(s)}, \tag{27}$$

where

$$\hat{W}^{(s)}(\lambda(r)) = W^{(s)}(1/\lambda(r), \lambda(r), 1), \tag{28}$$

so that from $(25)_1$, we finally obtain

$$T_\theta^{(s)}(r) = \frac{2\bar{\theta}}{l_0} r(\hat{W}^{(s)})' + \hat{W}^{(s)} + \gamma^{(s)}, \tag{29}$$

where the prime denotes, now, differentiation with respect to λ and $\gamma^{(s)}$ is an unknown integration constant.

Constants $\gamma^{(s)}$ $(s = 1, \ldots, N)$ and thickness $h^{(1)}$ can be calculated by imposing: (i) continuity of tractions at interfaces between layers ($N - 1$ equations) and (ii) traction boundary conditions at the external boundaries of the multilayer (two equations). Considering N layers, the traction continuity at the interfaces is written as

$$T_r^{(s-1)}(r_i^{(s-1)} + h^{(s-1)}) = T_r^{(s)}(r_i^{(s)}) \quad (s = 2, \ldots, N), \tag{30}$$

while null loading at the external surfaces of the multilayer yields

$$T_r^{(1)}(r_i^{(1)}) = 0, \quad T_r^{(N)}(r_i^{(N)} + h^{(N)}) = 0. \tag{31}$$

Therefore, $\gamma^{(N)}$ can be calculated from $(31)_2$

$$\gamma^{(N)} = -\hat{W}^{(N)}(\lambda(r_i^{(N)} + h^{(N)})), \tag{32}$$

while employing (30), we obtain the recursive formulae

$$\gamma^{(s-1)} = \hat{W}^{(s)}(\lambda(r_i^{(s)})) - \hat{W}^{(s-1)}(\lambda(r_i^{(s)})) + \gamma^{(s)} \quad (s = 2, \ldots, N). \tag{33}$$

Considering now $(31)_1$ and evaluating $\gamma^{(1)}$ from (33) written for $s = 2$, we obtain an implicit expression to be solved for $h^{(1)}$

$$\hat{W}^{(2)}(\lambda(r_i^{(2)})) - \hat{W}^{(1)}(\lambda(r_i^{(2)})) + \hat{W}^{(1)}(\lambda(r_i^{(1)})) + \gamma^{(2)} = 0, \tag{34}$$

where $h^{(2)}$ and $\gamma^{(2)}$ are functions of $h^{(1)}$ through (21) and (33), respectively.

Note that if the strain-energy function is the same for all layers, the multilayer corresponds to a homogeneous elastic block with thickness equal to the sum of all $h^{(s)}$; in this case, (33) shows that $\gamma^{(s)} = \gamma^{(N)}$, for every s, and the uniform layer solution is recovered.

4. Examples of multilayered plates under finite bending

The solution obtained in the previous section is interesting in itself and can be easily used for design purposes since it allows determination of the complex stress and strain fields within a thick, multilayered plate, when subject to finite bending. To highlight the usefulness of the solution, we present a few results for finite bending of an elastic thick plate, coated with a thin and stiff layer, and of a three- and five-layer structures, assuming a neo-Hookean behaviour for both materials.

Deformed geometries for the coated layer (with $l_0/h_0 = 2$, $h_0^{(\mathrm{lay})}/h_0^{(\mathrm{coat})} = 10$ and $\mu^{(\mathrm{coat})}/\mu^{(\mathrm{lay})} = 20$) are shown in Fig. 4, together with graphs of the dimensionless Cauchy principal stresses $T_r(r)/\mu^{(\mathrm{lay})}$

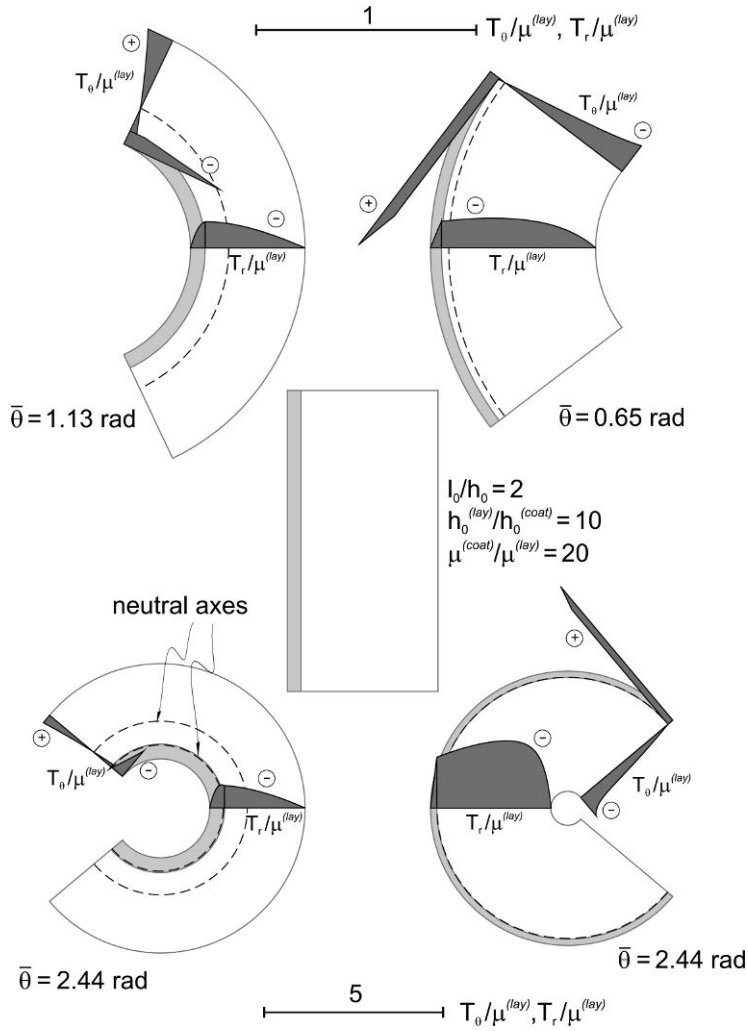

FIG. 4. Undeformed (centre) and deformed (upper and lower parts) shapes and internal stress states for finite bending of neo-Hookean coated plates with $l_0/h_0 = 2$, $h_0^{(\mathrm{lay})}/h_0^{(\mathrm{coat})} = 10$ and $\mu^{(\mathrm{coat})}/\mu^{(\mathrm{lay})} = 20$. Dashed lines represent the neutral axes. Note that in the picture in the lower part on the right, the neutral axis is almost coincident with the interface between the two layers, while on the left two neutral axes are visible. Note the scales of diagrams for dimensionless stresses.

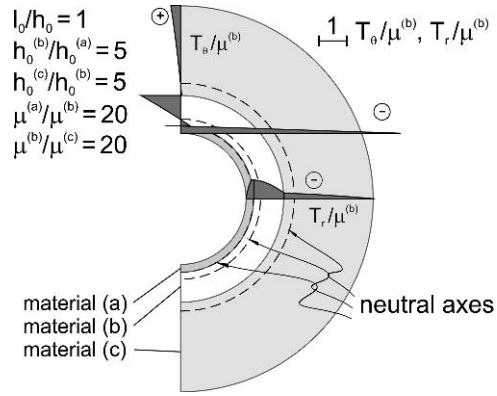

FIG. 5. Finite bending of a neo-Hookean three-layer plate showing three neutral axes.

and $T_\theta(r)/\mu^{(\mathrm{lay})}$. The deformed configurations plotted in the upper part of Fig. 4 correspond to critical configurations at bifurcation (see Section 6), while those reported in the lower part lie beyond the critical bifurcation threshold, so that they are reported only with the purpose to show the evolution of the solution of finite bending for very large angles. Note that the transverse stress is always compressive, while the distribution of $T_\theta(r)$ strongly depends on the stiffness of the layer under consideration and gives a null resultant, so that it is equivalent to the bending moment loading the plate. For all cases, the neutral axis (the line corresponding to vanishing circumferential stress) is drawn, showing the effect of the coating on the global stress state. Note that in the lower figure on the left, *two neutral axes* are visible. This is an important feature, which is also investigated in Fig. 5, referred to a three-layer plate. In this structure, where the initial aspect ratio is 1, the shear stiffness contrast is 20 and ratio between layer thicknesses is 5, *three neutral axes* become visible starting from a bending semi-angle of 56°, so that to give evidence to this effect a bending semi-angle of 90° is imposed in Fig. 5.

Finally, a complex situation with five layers with initial aspect ratio $l_0/h_0 = 4$ is reported in Fig. 6, where three configurations are shown at different bending angles $\bar{\theta}$. The layers are made up of two materials, *(a)* and *(b)*, such that $h_0^{(b)}/h_0^{(a)} = 3.5$ and $\mu^{(a)}/\mu^{(b)} = 10$. As in Fig. 4, the two principal components of the Cauchy stress are drawn. A peculiar feature of the stress state is the positive sign of the circumferential stress $T_\theta(r)$ in the inner, stiff layer, to be compared to the negative sign in the two adjacent layers. This situation once more confirms the presence of two neutral axes, one of which in this case is 'virtual', in the sense that it is obtained joining the 'peaks' of the diagram of the positive stresses.

5. Incremental bifurcations superimposed on finite bending of an elastic layered block

The goal of this section is to address the plane-strain bifurcation problem of the multilayered thick plate subject to finite bending, considered in Section 3. We begin by analysing the incremental field equations for an isolated layer and we continue formulating the multilayered problem by adding the relevant interfacial and external boundary conditions. We refer to Gei & Ogden (2002) for the notation.

The gradient of incremental displacement $\boldsymbol{u}(\boldsymbol{x})$ is

$$\boldsymbol{L} = u_{r,r}\boldsymbol{e}_r \otimes \boldsymbol{e}_r + \frac{u_{r,\theta} - u_\theta}{r}\boldsymbol{e}_r \otimes \boldsymbol{e}_\theta + u_{\theta,r}\boldsymbol{e}_\theta \otimes \boldsymbol{e}_r + \frac{u_r + u_{\theta,\theta}}{r}\boldsymbol{e}_\theta \otimes \boldsymbol{e}_\theta, \tag{35}$$

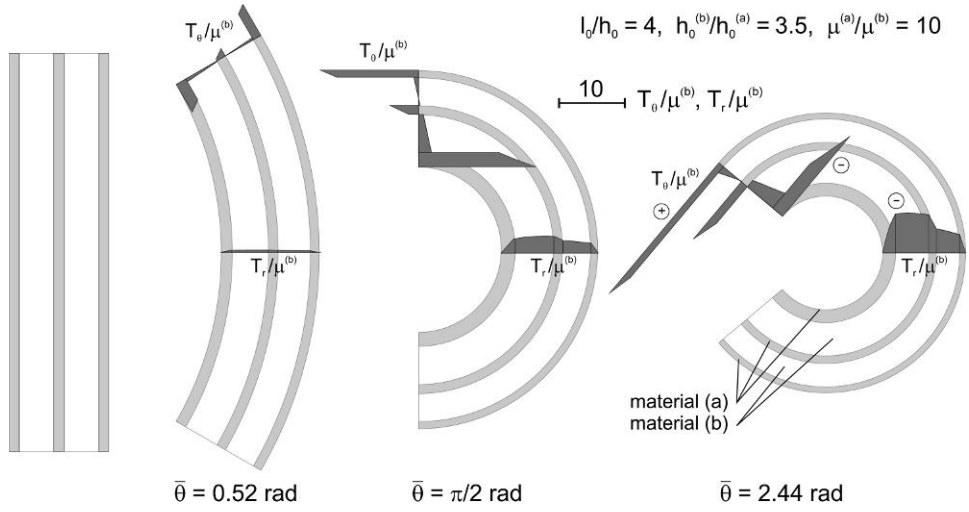

FIG. 6. From left to right: undeformed and progressively more deformed shapes and internal stress states for finite bending of a neo-Hookean five-layer plate with $l_0/h_0 = 4$, $h_0^{(b)}/h_0^{(a)} = 3.5$ and $\mu^{(a)}/\mu^{(b)} = 10$. Note the scales of diagrams for dimensionless stresses.

and the incompressibility condition ($\mathrm{tr}\boldsymbol{L} = 0$) can be written in polar coordinates as

$$r u_{r,r} + u_r + u_{\theta,\theta} = 0. \tag{36}$$

For an incompressible isotropic elastic material, the components of the constitutive fourth-order tensor $\mathbb{C}$ (see (6)) can be written as function of two incremental moduli, denoted μ and μ_*, that depend on the deformation. The non-vanishing components of $\mathbb{C}$ may be expressed as

$$\begin{aligned} &C_{rrrr} = C_{\theta\theta\theta\theta} = 2\mu_* + p, \quad C_{\theta r\theta r} = \mu - \Gamma, \\ &C_{r\theta r\theta} = \mu + \Gamma, \quad C_{r\theta\theta r} = C_{\theta rr\theta} = \mu + p, \end{aligned} \tag{37}$$

where

$$\Gamma = \frac{T_\theta - T_r}{2}, \quad p = -\frac{T_\theta + T_r}{2} \tag{38}$$

describe the state of prestress. For hyperelastic materials, μ and μ_* can be given in terms of the strain-energy function $\hat{W}(\lambda)$ as

$$\mu = \frac{\lambda}{2}\left(\frac{\lambda^4+1}{\lambda^4-1}\frac{\mathrm{d}\hat{W}}{\mathrm{d}\lambda}\right), \quad \mu_* = \frac{\lambda}{4}\left(\frac{\mathrm{d}\hat{W}}{\mathrm{d}\lambda} + \lambda\frac{\mathrm{d}^2\hat{W}}{\mathrm{d}\lambda^2}\right). \tag{39}$$

The incremental constitutive equations in terms of the incremental first Piola–Kirchhoff stress tensor can be written as

$$\begin{aligned} &\Sigma_{rr} = -\dot{\pi} + (2\mu_* + p)u_{r,r}, \quad \Sigma_{\theta\theta} = -\dot{\pi} + (2\mu_* + p)\frac{u_r + u_{\theta,\theta}}{r}, \\ &\Sigma_{r\theta} = (\mu + \Gamma)\frac{u_{r,\theta} - u_\theta}{r} + (\mu + p)u_{\theta,r}, \quad \Sigma_{\theta r} = (\mu + p)\frac{u_{r,\theta} - u_\theta}{r} + (\mu - \Gamma)u_{\theta,r}. \end{aligned} \tag{40}$$

A substitution of (40) and the use of $(25)_1$ in the incremental equations of equilibrium

$$\begin{aligned} \Sigma_{rr,r} + \frac{1}{r}\Sigma_{r\theta,\theta} + \frac{\Sigma_{rr} - \Sigma_{\theta\theta}}{r} = 0, \\ \Sigma_{\theta r,r} + \frac{1}{r}\Sigma_{\theta\theta,\theta} + \frac{\Sigma_{\theta r} + \Sigma_{r\theta}}{r} = 0, \end{aligned} \tag{41}$$

yields the incremental equilibrium equations expressed in terms of incremental displacements and in-plane mean stress

$$\begin{aligned} \dot{\pi}_{,r} &= \left\{(p + 2\mu_*)_{,r} + \frac{2(p + 2\mu_*)}{r}\right\} u_{r,r} + (p + 2\mu_*)u_{r,rr} \\ &\quad + (\mu + \Gamma)\frac{u_{r,\theta\theta} - u_{\theta,\theta}}{r^2} + (p + \mu)\frac{u_{\theta,r\theta}}{r}, \\ \dot{\pi}_{,\theta} &= [r(\mu - \Gamma)_{,r} + \mu - \Gamma]\left(u_{\theta,r} + \frac{u_{r,\theta} - u_\theta}{r}\right) + r(\mu - \Gamma)u_{\theta,rr} + (\mu - 2\mu_*)u_{r,\theta r}. \end{aligned} \tag{42}$$

We seek bifurcations in the following separable variables form

$$\begin{cases} u_r(r,\theta) = f(r)\cos n\theta, \\ u_\theta(r,\theta) = g(r)\sin n\theta, \\ \dot{\pi}(r,\theta) = k(r)\cos n\theta, \end{cases} \tag{43}$$

where $f(r)$, $g(r)$ and $k(r)$ are real functions and n is a real number to be determined by imposing boundary conditions.

Consideration of the incompressibility constraint

$$g = -\frac{(f + rf')}{n}, \tag{44}$$

and substitution of representations (43) into (42) yields

$$\begin{aligned} k' &= Df'' + \left(C_{,r} + D_{,r} + \frac{C + 2D}{r}\right) f' + \frac{E(1 - n^2)}{r^2} f, \\ k &= \frac{r^2 C}{n^2} f''' + \frac{F + 3C}{n^2} r f'' + \left(\frac{F}{n^2} - D\right) f' - \frac{1 - n^2}{n^2}\frac{F}{r} f, \end{aligned} \tag{45}$$

where a prime denotes differentiation with respect to r and in terms of incremental moduli μ and μ_* and strain-energy function $\hat{W}(\lambda)$, the coefficients C, D, E and F can be expressed as

$$\begin{aligned} C = \mu - \Gamma = \frac{\lambda}{\lambda^4 - 1}\frac{\mathrm{d}\hat{W}}{\mathrm{d}\lambda}, \quad D = 2\mu_* - \mu = \frac{\lambda}{2}\left(\lambda\frac{\mathrm{d}^2\hat{W}}{\mathrm{d}\lambda^2} - \frac{2}{\lambda^4 - 1}\frac{\mathrm{d}\hat{W}}{\mathrm{d}\lambda}\right), \\ E = \mu + \Gamma = \frac{\lambda^5}{\lambda^4 - 1}\frac{\mathrm{d}\hat{W}}{\mathrm{d}\lambda}, \quad F = rC_{,r} + C. \end{aligned} \tag{46}$$

By differentiating $(45)_2$ with respect to r and substituting it into $(45)_1$, a single differential equation in terms of $f(r)$ is obtained

$$\begin{aligned} &Cr^4 f'''' + 2(F+2C)r^3 f''' + [(rF)_{,r} + 4F - 2n^2 D]r^2 f'' \\ &+[(rF - 2rn^2 D)_{,r} - 2F]rf' + (1-n^2)(F - rF_{,r} - n^2 E) f = 0. \end{aligned} \tag{47}$$

Equation (47) defines the function $f(r)$ within a generic layer. Once $f(r)$ is known, the other functions, $g(r)$ and $k(r)$, can be calculated by employing (44) and $(45)_2$, respectively. The set of all functions $f^{(s)}(r)$ $(s = 1, \ldots, N)$ can be obtained imposing the continuity conditions at the interfaces and the boundary conditions at the external surfaces.

Continuity of incremental tractions and displacements at interfaces corresponds to

$$\begin{aligned} &u_r^{(s)}\Big|_{r=r_e^{(s)}} = u_r^{(s+1)}\Big|_{r=r_i^{(s+1)}}, \quad u_\theta^{(s)}\Big|_{r=r_e^{(s)}} = u_\theta^{(s+1)}\Big|_{r=r_i^{(s+1)}}, \\ &\Sigma_{rr}^{(s)}\Big|_{r=r_e^{(s)}} = \Sigma_{rr}^{(s+1)}\Big|_{r=r_i^{(s+1)}}, \quad \Sigma_{\theta r}^{(s)}\Big|_{r=r_e^{(s)}} = \Sigma_{\theta r}^{(s+1)}\Big|_{r=r_i^{(s+1)}}, \end{aligned} \tag{48}$$

where $r_e^{(s)} = r_i^{(s)} + h^{(s)}$ or, in terms of functions defined in (43),

$$\begin{aligned} &f^{(s)}\Big|_{r=r_e^{(s)}} = f^{(s+1)}\Big|_{r=r_i^{(s+1)}}, \quad g^{(s)}\Big|_{r=r_e^{(s)}} = g^{(s+1)}\Big|_{r=r_i^{(s+1)}}, \\ &\{(p+2\mu_*)f' - k\}^{(s)}\Big|_{r=r_e^{(s)}} = \{(p+2\mu_*)f' - k\}^{(s+1)}\Big|_{r=r_i^{(s+1)}}, \\ &\left\{Cg' - \frac{1}{r}(nf+g)(p+\mu)\right\}^{(s)}\Big|_{r=r_e^{(s)}} = \left\{Cg' - \frac{1}{r}(nf+g)(p+\mu)\right\}^{(s+1)}\Big|_{r=r_i^{(s+1)}}. \end{aligned} \tag{49}$$

For dead-load tractions on the external surfaces, the boundary conditions at $r = r_i^{(1)}$ and $r = r_e^{(N)}$ are

$$\Sigma_{rr}^{(1),(N)}\Big|_{r=r_i^{(1)}, r_e^{(N)}} = 0, \quad \Sigma_{\theta r}^{(1),(N)}\Big|_{r=r_i^{(1)}, r_e^{(N)}} = 0, \tag{50}$$

or, equivalently,

$$\begin{aligned} &\{(p+2\mu_*)f' - k\}^{(1),(N)}\Big|_{r=r_i^{(1)}, r_e^{(N)}} = 0, \\ &\left\{Cg' - \frac{1}{r}(nf+g)(p+\mu)\right\}^{(1),(N)}\Big|_{r=r_i^{(1)}, r_e^{(N)}} = 0. \end{aligned} \tag{51}$$

On the boundaries $\theta = \pm\bar{\theta}$, we require that shear stresses and incremental normal displacements vanish, namely

$$\Sigma_{r\theta}^{(s)}\Big|_{\theta=\pm\bar{\theta}} = 0, \quad u_\theta^{(s)}\Big|_{\theta=\pm\bar{\theta}} = 0, \tag{52}$$

a condition which is achieved if $\sin n\bar{\theta} = 0$ (see (43)) or, equivalently, using (17), if

$$n = \frac{2m\pi}{\alpha l_0} \quad (m \in \mathbb{N}). \tag{53}$$

Since our objective is to employ a numerical method to evaluate the critical angle for bifurcation $\bar{\theta}_{\rm cr}$, it becomes instrumental to rewrite (47) as a linear system of first-order ordinary differential equations. This and the procedure to derive numerically the bifurcation condition is described in Appendix A.

Equation (A.15) provides the critical angle for bifurcation, $\bar{\theta}_{\rm cr}$, for a multilayered elastic plate subject to bending in terms of initial aspect ratios and stiffness contrast between layers. Once this angle is known, equation $(20)_2$ yields the critical stretch $\lambda_{\rm cr} = 2\bar{\theta}_{\rm cr} r_i^{(1)}/l_0$.

6. An example: bifurcation of a bilayer

Although our analysis covers the case of a N-layer system, we will limit examples to the simple geometry of a two-layered system, also experimentally investigated, where one of the layers is taken thin and rigid with respect to the other, so that it acts as a sort of stiff coating. Both layers are made up of neo-Hookean material (for which the response always remains elliptic).

The critical angle $\bar{\theta}_{\rm cr}$ and the critical stretch $\lambda_{\rm cr}$ (at the compressive side of the specimen) at bifurcation are reported in Figs 7 and 8 as functions of the aspect ratio l_0/h_0 (unloaded height of the specimen is l_0 and global thickness is h_0, see Fig. 3), for the thickness and stiffness ratios $h_0^{(\rm lay)}/h_0^{(\rm coat)} = 10$ and $\mu^{(\rm coat)}/\mu^{(\rm lay)} = 20$, respectively. In the figures, bifurcation curves are reported for different values of the integer parameter m which, through (53), defines the circumferential wave number n. Obviously, for a given value of l_0/h_0, the bifurcation threshold is set by the value of m providing the minimum (or maximum) value of the critical angle (or stretch). The difference between Figs 7 and 8 is that the coating layer is at the tensile side of the specimen in the former case while it is at the compressive side in the latter.

In the same figures, also the threshold is reported for surface instability of the 'soft' layer material ($\lambda_{\rm surf} \approx 0.545$, see Biot, 1965). It can be deduced from the figures that a diffuse mode setting the bifurcation threshold always exists before surface instability, for each aspect ratio l_0/h_0[6]. It is important to observe that the occurrence of the critical diffuse mode is very close to the surface instability when the coating is located at the tensile side of the specimen (Fig. 7), while the two thresholds become well separated in the other case, namely, when the coating is located at the compressive side (Fig. 8). This is because, in the latter, bifurcation takes place with a buckling-like mode in the coating, then occurring at a limitated axial stretch in the stiff layer. We can also observe from Fig. 7 (Fig. 8) that for $l_0/h_0 > 10$ (for $l_0/h_0 > 6$), the coated structures can be bent to the annular configuration without 'encountering' any instability.

Some typical configurations and stress distributions at bifurcation corresponding to $l_0/h_0 = 2$ in Figs 7 and 8 (indicated by small 'square symbols' on the bifurcation curve) are sketched in Fig. 4 for both positions of the stiff layer.

The critical angle at bifurcation is reported in Figs 9 and 10 as a function of the aspect ratio l_0/h_0 for two values of coating thickness, $h_0^{(\rm lay)}/h_0^{(\rm coat)} = \{10, 20\}$ when the coating layer is on the tensile and on the compressive side, respectively. In the same figures, the case of the uncoated layer is also reported for comparison.

Note that results reported in Fig. 9 are similar to those reported in Fig. 2 since the coating is in the same position, though the stiffness ratio between coating and layer is different and equal to 20 in the former case and 500 in the latter.

[6]For a single elastic block, Triantafyllidis (1980) claims that surface instability occurs before diffuse modes, while Coman & Destrade (2008) on the contrary demonstrate that the first instability mode is diffused. However, the two points of view can be reconciled since for a single layer the surface instability and the instability in diffused modes are very close and may be taken to coincide in a first approximation.

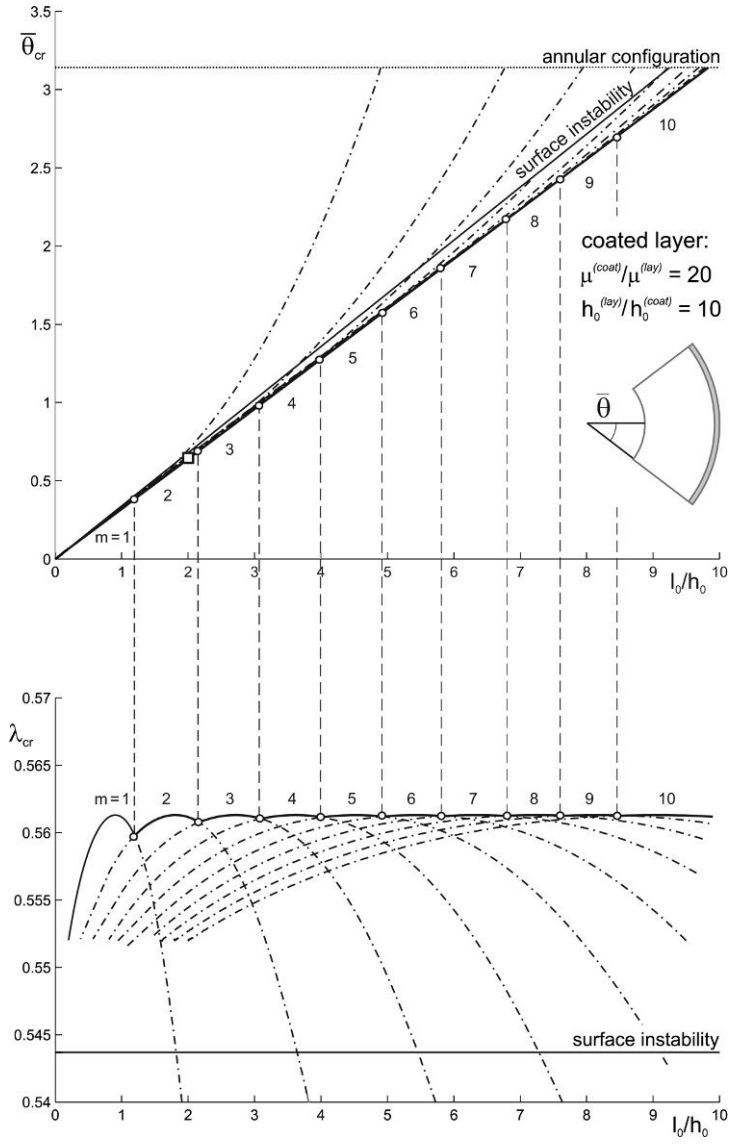

FIG. 7. Critical angle $\bar{\theta}_{\rm cr}$ and critical stretch $\lambda_{\rm cr}$ (evaluated at the internal boundary, $r = r_i^{(1)}$) versus aspect ratio l_0/h_0 of a neo-Hookean coated bilayer subject to bending with $h_0^{(\rm lay)}/h_0^{(\rm coat)} = 10$ and $\mu^{(\rm coat)}/\mu^{(\rm lay)} = 20$. The coating is located at the tensile side. In both plots, a small circle denotes a transition between two different integer values of m (the parameter which sets the circumferential wave number). The small 'square' on the bifurcation curve indicates the configuration studied in Fig. 4, top-left position.

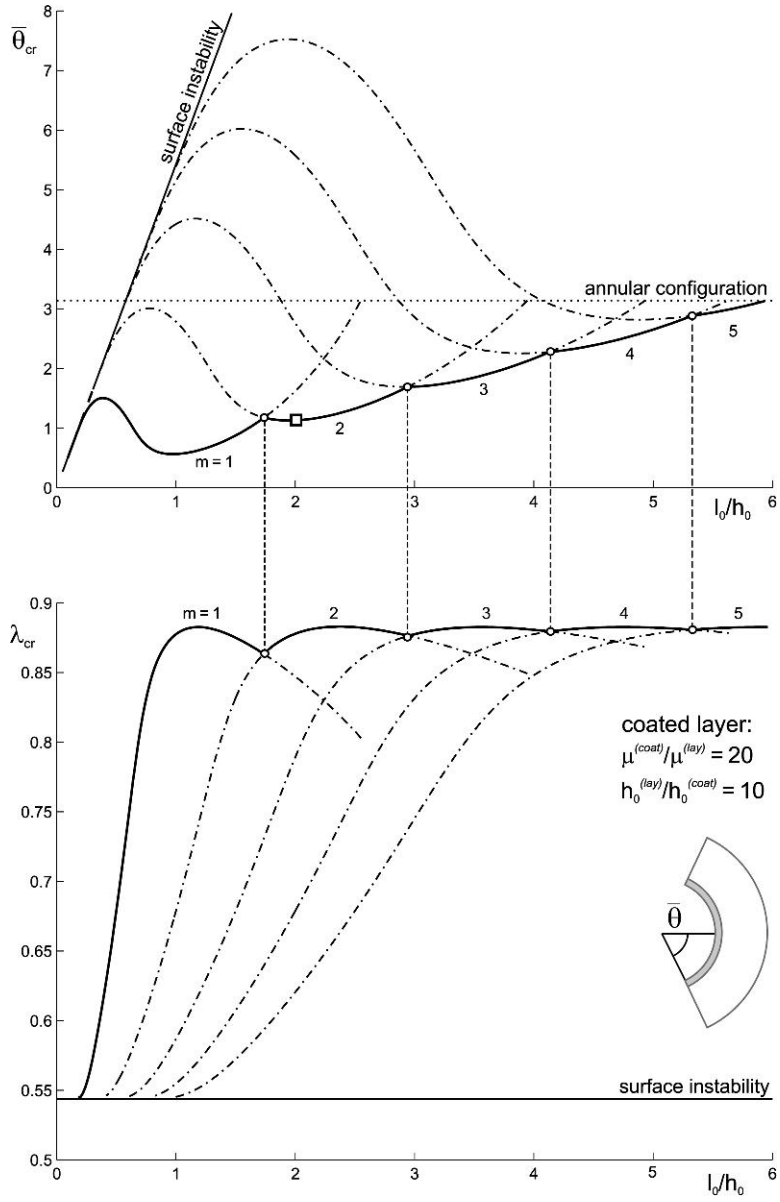

FIG. 8. Critical angle $\bar{\theta}_{cr}$ and critical stretch λ_{cr} (evaluated at the internal boundary, $r = r_i^{(1)}$) versus aspect ratio l_0/h_0 of a neo-Hookean coated bilayer subject to bending with $h_0^{(lay)}/h_0^{(coat)} = 10$ and $\mu^{(coat)}/\mu^{(lay)} = 20$. The coating is located at the compressed side. In both plots, a small circle denotes a transition between two integer values of m (the parameter which sets the circumferential wave number). The small 'square' on the bifurcation curve indicates the configuration studied in Fig. 4, top-right position.

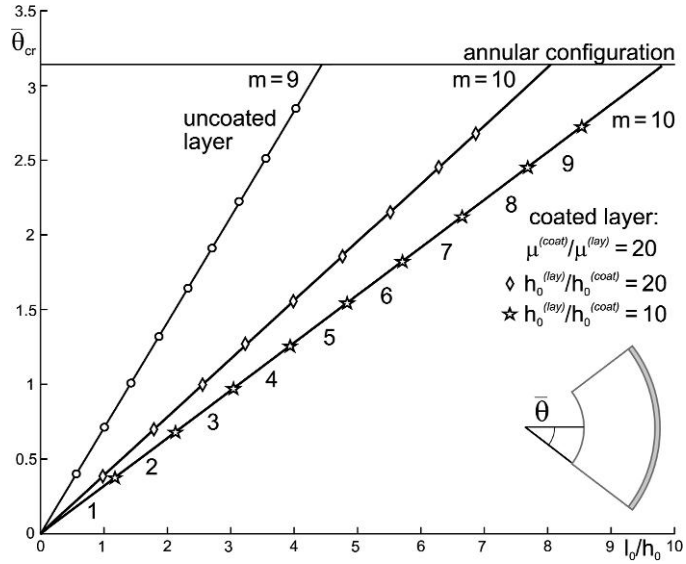

FIG. 9. Comparison between the critical angle $\bar{\theta}_{\rm cr}$ at bifurcation versus aspect ratio l_0/h_0 of two neo-Hookean coated bilayers subject to bending with coating at the tensile side with $\mu^{(\rm coat)}/\mu^{(\rm lay)} = 20$ and $h_0^{(\rm lay)}/h_0^{(\rm coat)} = 10$ and 20, respectively. In every curve, a small symbol denotes a transition between two different integer values of m (the parameter which sets the circumferential wave number). Bifurcation angles for a single, uncoated layer are also reported.

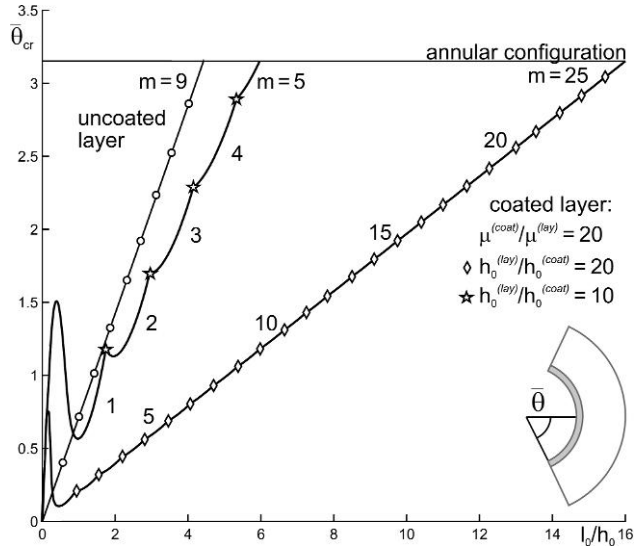

FIG. 10. Comparison between the critical angle $\bar{\theta}_{\rm cr}$ at bifurcation versus aspect ratio l_0/h_0 of two neo-Hookean coated bilayers subject to bending with coating at the compressed side with $\mu^{(\rm coat)}/\mu^{(\rm lay)} = 20$ and $h_0^{(\rm lay)}/h_0^{(\rm coat)} = 10$ and 20, respectively. In every curve, a small symbol denotes a transition between two different integer values of m (the parameter which sets the circumferential wave number). Bifurcation angles for a single, uncoated layer are also reported.

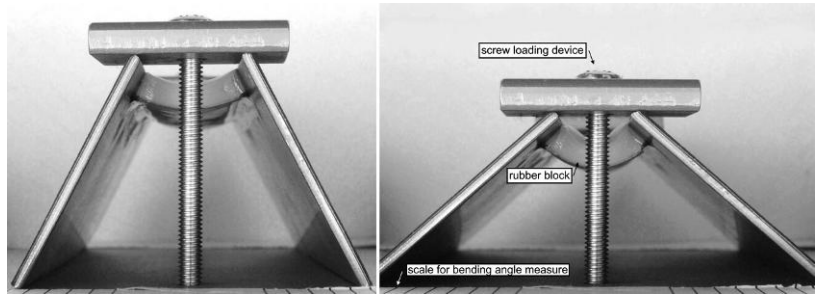

FIG. 11. Device used to impose finite bending (of a semi-angle $\bar{\theta}$ equal to 25° on the left and to 45° on the right, with reference to Fig. 3) to coated and uncoated rubber strips (an uncoated 10 × 100 × 4 mm^3 rubber strip is subject to bending in the photo).

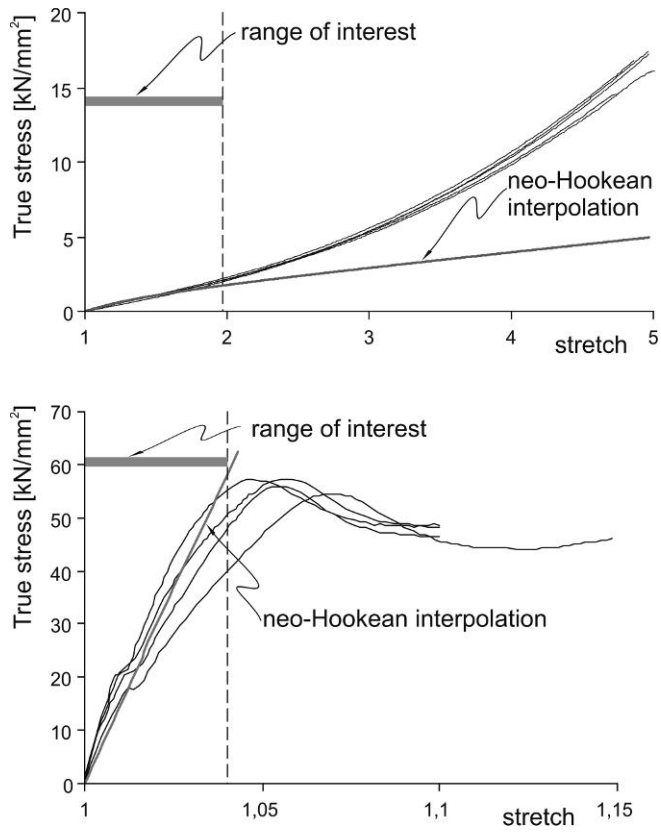

FIG. 12. Uniaxial tests on and material characterizations of the natural rubber and the polyester film employed in the specimens. Note that the neo-Hookean interpolation has been selected to be valid only within the 'range of interest' to experimentally detected bifurcations.

It is evident from the figures that the bifurcation solution for a single layer is approximated by a straight line, so that we can write down the approximated solution

$$\bar{\theta}_{\rm cr} = 0.712\, l_0/h_0, \tag{54}$$

which has passed unnoted until the present work.

We may also note that a linear relation between $\bar{\theta}_{\rm cr}$ and l_0/h_0 is also evident in the cases of Figs 2, 7 and 9, while such a linear relation holds only at high values of l_0/h_0 in the cases of Figs 8 and 10. Moreover, the inclination of such lines depends on the elastic and thickness contrasts between layers, so that a simple formula like (54) is hard to be obtained.

7. Bifurcation experiments on coated and uncoated rubber strips

To substantiate our theoretical results, we have designed and performed experiments, following the approach initiated by Gent & Cho (1999) (see also Gent, 2005). In particular, we have imposed a finite bending to uncoated and coated elastic strips (made of natural rubber), employing the device shown in Fig. 11, in which a rubber strip is glued to two metallic platelets along the longer sides (using Loctite ©) and these platelets are forced to impose a bending to the strip, using a simple screw-loading device. Two different coatings have been tested, both realized using 0.2 mm thick polyester transparent films (commercial copier films), glued singular or double (using Loctite ©) to the rubber strip. During finite bending, the appearance of crazes has been detected by direct visual inspection.

The natural rubber and the polyester films (4 dog-bone shaped standard ISO 5277-1/1BA 30 × 5 mm^2 samples for each material) have been tested under uniaxial stress, thus obtaining the results shown in Fig. 12, where the true stress is plotted versus the stretch. It may be interesting to note that, while the response of the rubber is typical of these materials, the stress/stretch curve of the polyester film is highly non-linear, exhibiting a peak and a softening regime. In the plots, the interpolation with the neo-Hookean material selected for the calculations is also included (giving $\mu^{(\rm lay)} \simeq 1$ kN/mm^2 and $\mu^{(\rm coat)} \simeq 500$ kN/mm^2). This interpolation curve may seem poor at a first glance, but we should point out that all the bifurcations found in the experiments have occurred with maximum stretches ranging between 1.52 and 1.9 (1.38 and 1.64 for samples with thick coating) in the rubber and between 1.02 and 1.04 (1.01 and 1.02 for samples with thick coating) in the polyester. For this reason, the selected neo-Hookean interpolation is much more accurate than it may appear and is taken valid either in tension or in compression.

The progression of bending is shown in Fig. 13, referred to a 20 × 4 × 100 mm^3 rubber strip coated with two 0.2 mm thick films (in which the larger dimension is that out-of-plane, taken sufficiently large to simulate the plane strain condition). At a certain stage of finite bending, namely, at a certain bending semi-angle $\bar{\theta}_{\rm cr}$, crazes can be detected to appear on the surface of the sample. This circumstance has been identified with appearance of small wavelength bifurcations[7] and compared with theoretical predictions for uncoated layers and for layers with a stiff coating at the tensile side of the specimen.

Details of the surface of the block suffering compression are reported in Fig. 14 at different bending semi-angles (30°, 40°, 50°) from which we may note that crazes appear at an opening semi-angle lying between 30° and 40°.

[7]Theoretical predictions indicate that the critical mode is always a diffuse mode, which—for obvious reasons—cannot be detected by direct visual inspection. However, for the geometries tested by us (an uncoated layer and layers coated at the side under tension), this mode is very close to a high-wave number mode, which is that detected by visual inspection.

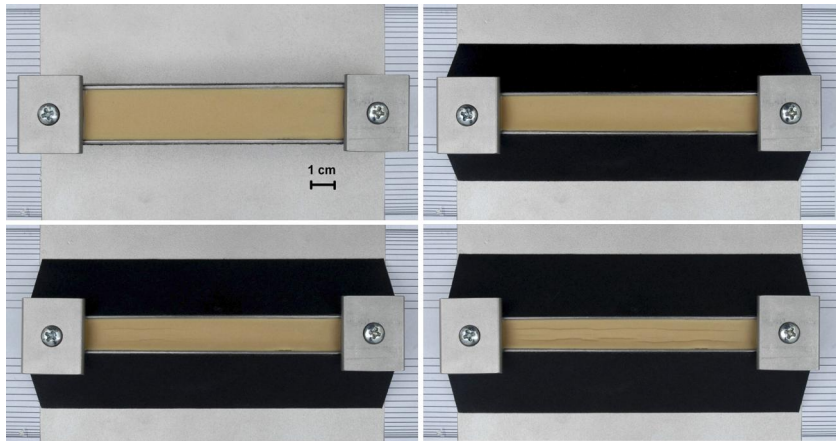

FIG. 13. Finite bending of a $20 \times 4 \times 100$ mm^3 rubber block coated with two polyester 0.2 mm thick films, imposed with the device shown in Fig. 11. From the top to the bottom, left to right: specimen before loading; specimen bent at a semi-angle of 30° (crazes are still not visible, see the detail reported in Fig. 14); specimen bent at a semi-angle of 40° (crazes become visible, see the detail reported in Fig. 14); specimen bent at a semi-angle of 50° (crazes invade the whole specimen, see the detail reported in Fig. 14).

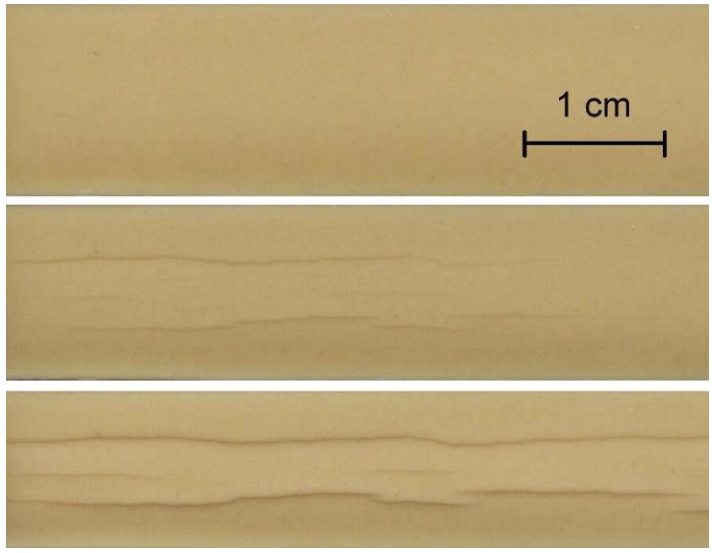

FIG. 14. Details of Fig. 13. Crazes become visible in the photo taken at an opening semi-angle of 40° (centre) and invade the whole sample at 50° (lower part), while these remain undetected at 30° (upper part).

The results of experiments and theoretical predictions are summarized in Table 1, where bifurcation semi-angles are reported for the different geometries tested, and in Fig. 2. Despite the fact that our loading device does not exactly impose the correct boundary conditions on the planar sizes of the bent specimen (where the specimen should be free of sliding), the experimental results are in a fairly well agreement with the theoretical predictions (with a tendency towards overestimation of bifurcation

TABLE 1 *Summary of experimental results (in terms of critical semi-angle at bifurcation, $\bar{\theta}_{cr}^{exp}$) and theoretical predictions ($\bar{\theta}_{cr}$) (the percentage error is denoted by 'err.') for rubber samples of thickness $h_0^{(lay)} = 4$ mm, uncoated and coated with a stiff 0.2 mm or 0.4 mm coating. $\bar{\theta}_{cr} = 180^\circ$ means that the annular configuration can be reached without bifurcation*

l_0	$h_0^{(coat)} = 0$		$h_0^{(coat)} = 0.2$ mm			$h_0^{(coat)} = 0.4$ mm		
mm	$\bar{\theta}_{cr}^{exp}$	$(\bar{\theta}_{cr})$	$\bar{\theta}_{cr}^{exp}$	$(\bar{\theta}_{cr})$	*err.* [%]	$\bar{\theta}_{cr}^{exp}$	$(\bar{\theta}_{cr})$	*err.* [%]
10	58°	(101.99°)		—			—	
15	100°	(142.09°)	31°	(39.01°)	20.53	25°	(33.88°)	26.21
20	180°	(180°)	50°	(54.79°)	8.74	38°	(48.44°)	21.55
30	180°	(180°)	73°	(75.54°)	3.36	64°	(72.61°)	11.86
40	180°	(180°)	102°	(101.99°)	0.01	80°	(93.31°)	14.26
50	180°	(180°)	140°	(133.64°)	4.75	110°	(120.38°)	8.62

angles) in all cases of uncoated and coated (two coating thicknesses, 0.2 and 0.4 mm, have been investigated) strips.

8. Conclusions

A new plane strain solution for finite bending of a thick, elastic multilayered plate shows the complex stress state developing in multilayered structures subject to large strain (evidencing, for instance, two or three neutral axes). This solution allows treatment of 2D bifurcations, revealing the strong influence on bifurcation load of geometry and stiffness contrast between layers. The predictions of bifurcation configuration have been confirmed by developing a simple experimental procedure, so that it may be concluded that the theory can be effectively used to predict limits to the deformation capability of multilayered materials.

Acknowledgment

Experiments have been conducted at the laboratory for Physical Modeling of Structures and Photoelasticity of the University of Trento, managed by D. Bigoni.

Funding

Progetto di Ricerca di Interesse Nazionale (2007YZ3B24) 'Multi-scale Problems with Complex Interactions in Structural Engineering' financed by Italian Ministry of University and Research.

REFERENCES

BIGONI, D. & GEI, M. (2001) Bifurcations of a coated, elastic cylinder. *Int. J. Solids Struct.*, **38**, 5117–5148.

BIOT, M. A. (1965) *Mechanics of Incremental Deformations*. New York: Wiley.

BRUHNS, O. T., GUPTA, N. K., MEYERS, A. T. M. & XIAO, H. (2003) Bending of an elastoplastic strip with isotropic and kinematic hardening. *Arch. Appl. Mech.*, **72**, 759–778.

BRUHNS, O. T., XIAO, H. & MEYERS, A. (2002) Finite bending of a rectangular block of an elastic Hencky material. *J. Elast.*, **66**, 237–256.

CHU, S. N. G. (1998) Elastic bending of semiconductor wafer revisited and comments on Stoney's equation. *J. Electrochem. Soc.*, **145**, 3621–3627.

CHUANG, T. J. & LEE, S. (2000) Elastic flexure of bilayered beams subject to strain differentials. *J. Mater. Res.*, **15**, 2780–2788.

COMAN, C. D. & DESTRADE, M. (2008) Asymptotic results for bifurcations in pure bending of rubber blocks. *Q. J. Mech. Appl. Math.*, **61**, 395–414.

DRYBURGH, G. & OGDEN, R. W. (1999) Bifurcation of an elastic surface-coated incompressible isotropic elastic block subject to bending. *Z. Angew. Math. Phys.*, **50**, 822–838.

FAN, Z., RAZAVI, H., DO, J., MORIKAWI, A., ERGEN, O., CHUEH, Y.-L., LEU, P. W., HO, J. C., TAKAHASHI, T., REICHERTZ, L. A., NEALE, S., YU, K., WU, M., AGER, J. W. & JAVEY, A. (2009) Three-dimensional nanopillar-array photovoltaics on low-cost and flexible substrates. *Nat. Mater.*, **8**, 648–653.

GEI, M. & OGDEN, R. W. (2002) Vibration of a surface-coated elastic block subject to bending. *Math. Mech. Solids*, **7**, 607–628.

GENT, A. N. (2005) Elastic instabilities in rubber. *Int. J. Nonlinear Mech.*, **40**, 165–175.

GENT, A. N. & CHO, I. S. (1999) Surface instabilities in compressed or bent rubber blocks. *Rubber Chem. Technol.*, **72**, 253–262.

GREEN, A. E. & ZERNA, W. (1968) *Theoretical Elasticity*. London: Oxford University Press.

HAUGHTON, D. M. (1999) Flexure and compression of incompressible elastic plates. *Int. J. Eng. Sci.*, **37**, 1693–1708.

L'HEUREUX, N., DUSSERRE, N., KONIG, G., VICTOR, B., KEIRE, P., WIGHT, T. N., CHRONOS, N. A. F., KYLES, A. E., GREGORY, C. R., HOYT, G., ROBBINS, R. C. & MCALLISTER, T. N. (2006) Human tissue-engineered blood vessel for adult arterial revascularization. *Nat. Med.*, **12**, 361–365.

LINDSAY, K. A. (1992) The application of compound matrices to convection problems in multi-layered continua. *Math. Models Methods Appl. Sci.*, **2**, 121–141.

LINDSAY, K. A. & ROONEY, C. E. (1992) A note on compound matrices. *J. Comput. Phys.*, **103**, 472–477.

LURIE, A. I. (2005) *Theory of Elasticity*. New York: Springer.

RIVLIN, R. S. (1949) Large elastic deformations of isotropic materials. V. The problem of flexure. *Proc. R. Soc. Lond.* A, **195**, 463–473.

TRIANTAFYLLIDIS, N. (1980) Bifurcation phenomena in pure bending. *J. Mech. Phys. Solids*, **28**, 221–245.

TRUESDELL, C. & TOUPIN, R. A. (1960) The classical field theories. *Encyclopedia of Physics* (S. Flügge eds), vol. III/1. Berlin: Springer.

Appendix A. Numerical procedure to seek the critical angle $\bar{\theta}_{\rm cr}$ at bifurcation

The bifurcation condition can be numerically determined by introducing, for each layer, the vector

$$[z](r) = [\, f(r) \quad f'(r) \quad f''(r) \quad f'''(r)]^{\top}, \tag{A.1}$$

so that the differential equations (47) can be rewritten as

$$[z'] = [A][z], \tag{A.2}$$

where the matrix $[A]$ takes the form

$$[A] = \begin{bmatrix} 0 & 1 & 0 & 0 \\ 0 & 0 & 1 & 0 \\ 0 & 0 & 0 & 1 \\ -A_{41} & -A_{42} & -A_{43} & -A_{44} \end{bmatrix}, \tag{A.3}$$

with

$$\begin{aligned} A_{41}(r) &= (1-n^2)(F - rF_{,r} - n^2E)/(Cr^4), \\ A_{42}(r) &= [(rF + 2rn^2D)_{,r} - 2F]/(Cr^3), \\ A_{43}(r) &= [(rF)_{,r} + 4F - 2n^2D]/(Cr^2), \\ A_{44}(r) &= 2(F + 2C)/(Cr). \end{aligned} \tag{A.4}$$

Adopting the notation $[X^{(s)}]_e = [X^{(s)}](r_e^{(s)})$ and $[X^{(s)}]_i = [X^{(s)}](r_i^{(s)})$ for vectors or matrices referred to a generic layer s, and using (44–45), the continuity of incremental tractions and displacements at an interface between layers, (49), can be represented in matrix form as

$$\begin{bmatrix} [Q^{(s)}]_e & -[Q^{(s+1)}]_i \end{bmatrix} \begin{bmatrix} [z^{(s)}]_e \\ [z^{(s+1)}]_i \end{bmatrix} = [0], \tag{A.5}$$

where

$$[Q](r) = \begin{bmatrix} F(n^2-1) & r[F - n^2(2D + C - T_r)] & r^2(F + 3C) & r^3C \\ (n^2-1)(C - T_r) & r(C + T_r) & r^2C & 0 \\ 1 & 0 & 0 & 0 \\ 1 & r & 0 & 0 \end{bmatrix}, \tag{A.6}$$

while boundary conditions (51) can conveniently be rewritten as

$$[B^{(1)}]_i\,[z^{(1)}]_i = [0], \quad [B^{(N)}]_e\,[z^{(N)}]_e = [0], \tag{A.7}$$

where

$$[B](r) = \begin{bmatrix} F(n^2-1) & r[F - n^2(2D + C)] & r^2(F + 3C) & r^3C \\ n^2-1 & r & r^2 & 0 \end{bmatrix}. \tag{A.8}$$

We are now in a position to set the numerical solution procedure. Since in our examples we have always addressed systems with few layers, we use the simple following numerical procedure. However, for multilayered domains, the so-called 'compound matrix method' (Lindsay, 1992; Lindsay & Rooney, 1992) would be particularly suited. This method has also been implemented confirming our results.

(1) Employing a numerical integration based on an explicit Runge–Kutta (4,5)-formula, we solve, for each layer (index s has been dropped for simplicity), four initial-value problems. These are based on system (A.2), with the following four initial conditions:

$$\begin{aligned} [z_{(1)}]_i &= [1\ 0\ 0\ 0]^\top, \quad [z_{(2)}]_i = [0\ 1\ 0\ 0]^\top, \\ [z_{(3)}]_i &= [0\ 0\ 1\ 0]^\top, \quad [z_{(4)}]_i = [0\ 0\ 0\ 1]^\top. \end{aligned}$$

In this way, we find four integrals,

$$[z_{(m)}](r) \quad (m = 1, \ldots, 4), \tag{A.9}$$

for each layer.

(2) The general solution for each layer can be constructed by linear combination of the four functions (A.9), so that we obtain

$$[z](r) = C_1[z_{(1)}](r) + C_2[z_{(2)}](r) + C_3[z_{(3)}](r) + C_4[z_{(4)}](r), \tag{A.10}$$

where the unknown constants C_i $(i = 1, \ldots, 4)$ set the amplitude of the bifurcation mode. These can be collected for each layer in a vector $[c] = [C_1\ C_2\ C_3\ C_4]^\top$.

(3) Boundary and interfacial conditions for the multilayer can be recast in matrix form as

$$\begin{bmatrix} [\hat{B}^{(1)}]_i & & : & & 0 \\ [\hat{Q}^{(1)}]_e & -[\hat{Q}^{(2)}]_i & : & & \\ & [\hat{Q}^{(1)}]_e & : & & \\ .. & .. & .. & .. & .. \\ & & : & [\hat{Q}^{(N-1)}]_e & -[\hat{Q}^{(N)}]_i \\ 0 & & : & & [\hat{B}^{(N)}]_e \end{bmatrix} \begin{bmatrix} [c^{(1)}] \\ [c^{(2)}] \\ .. \\ .. \\ [c^{(N-1)}] \\ [c^{(N)}] \end{bmatrix} = [0] \tag{A.11}$$

or equivalently as

$$[M][\hat{c}] = [0], \tag{A.12}$$

where

$$[\hat{B}^{(s)}]_{i,e} = \begin{bmatrix} B^{(s)}_{1j} z^{(s)}_{(1)j} & B^{(s)}_{1j} z^{(s)}_{(2)j} & B^{(s)}_{1j} z^{(s)}_{(3)j} & B^{(s)}_{1j} z^{(s)}_{(4)j} \\ B^{(s)}_{2j} z^{(s)}_{(1)j} & B^{(s)}_{2j} z^{(s)}_{(2)j} & B^{(s)}_{2j} z^{(s)}_{(3)j} & B^{(s)}_{2j} z^{(s)}_{(4)j} \end{bmatrix}_{r=r_i, r_e} \tag{A.13}$$

and

$$[\hat{Q}^{(s)}]_{i,e} = \begin{bmatrix} Q^{(s)}_{1j} z^{(s)}_{(1)j} & Q^{(s)}_{1j} z^{(s)}_{(2)j} & Q^{(s)}_{1j} z^{(s)}_{(3)j} & Q^{(s)}_{1j} z^{(s)}_{(4)j} \\ Q^{(s)}_{2j} z^{(s)}_{(1)j} & Q^{(s)}_{2j} z^{(s)}_{(2)j} & Q^{(s)}_{2j} z^{(s)}_{(3)j} & Q^{(s)}_{2j} z^{(s)}_{(4)j} \\ Q^{(s)}_{3j} z^{(s)}_{(1)j} & Q^{(s)}_{3j} z^{(s)}_{(2)j} & Q^{(s)}_{3j} z^{(s)}_{(3)j} & Q^{(s)}_{3j} z^{(s)}_{(4)j} \\ Q^{(s)}_{4j} z^{(s)}_{(1)j} & Q^{(s)}_{4j} z^{(s)}_{(2)j} & Q^{(s)}_{4j} z^{(s)}_{(3)j} & Q^{(s)}_{4j} z^{(s)}_{(4)j} \end{bmatrix}_{r=r_i, r_e}, \tag{A.14}$$

so that bifurcation corresponds to the condition that system (A.11) admits a non-trivial solution, namely,

$$\det[M] = 0, \tag{A.15}$$

which provides the critical semi-angle $\bar{\theta}_{\mathrm{cr}}$.